Research Papers

GREENSUSMATER

Greensusmater
Vol. 2, No. 2, 2025
https://doi.org/10.62755/greensusmater.2025.2.2.55-61

Check for updates

Development and Materials Characterization of Hydrothermally Grown Niobium-Doped $BiVO_4$ for Ciprofloxacin and Methylene Blue Degradation

Nadiya Rifqah Kurnia[1] Tia Amanda1[1] Rima Nurfitria[1] Rizky Aflaha[2] Januar Widakdo[3] Aditya Rianjanu[1,4]

[1] *Department of Materials Engineering, Faculty of Industrial Technology, Institut Teknologi Sumatera, Terusan Ryacudu, Way Hui, Jati Agung, Lampung Selatan, 35365 Indonesia*
[2] *Department of Physics, Faculty of Mathematics and Natural Sciences, Universitas Gadjah Mada, Sekip Utara, BLS 21, Yogyakarta 55281, Indonesia*
[3] *Department of Physics, Faculty of Mathematics and Natural Sciences, Universitas Indonesia, Depok 16424, Indonesia*
[4] *Center for Green and Sustainable Materials, Institut Teknologi Sumatera, Terusan Ryacudu, Way Hui, Jati Agung, Lampung 35365, Indonesia*

Corresponding author: aditya.rianjanu@mt.itera.ac.id (AR)

ARTICLE HISTORY: Received: October 02, 2025 | Revised: November 22, 2025 | Accepted: November 26, 2025

ABSTRACT

This study presents the synthesis and comprehensive characterization of niobium-doped bismuth vanadate (Nb_X-$BiVO_4$, $X = 0$, 2, 4, and 6 mol%) photocatalysts prepared via a hydrothermal method, with the objective of improving the degradation efficiency of organic contaminants under UV light irradiation. X-ray diffraction (XRD) confirmed the retention of the monoclinic $BiVO_4$ crystal structure across all samples, although slight secondary phases emerged in the doped variants. Field emission scanning electron microscopy (FESEM) revealed increasingly rough and nanostructured surface morphologies with higher Nb incorporation. Ultraviolet-visible (UV-Vis) and photoluminescence (PL) spectroscopic analyses demonstrated altered electronic band structures and suppressed charge carrier recombination. Photocatalytic activity was investigated using ciprofloxacin (CIP) and methylene blue (MB) as model pollutants. The Nb6-$BiVO_4$ sample exhibited the highest photocatalytic activity against CIP (rate constant $k = 0.09$ min^{-1} g^{-1}), attributed to enhanced charge separation and improved surface texturing. Conversely, MB degradation was most efficient with undoped $BiVO_4$ ($k = 0.29$ min^{-1} g^{-1}), likely due to superior dye adsorption, despite the optical enhancements seen in doped specimens. These results suggest that Nb doping enhances the photocatalytic performance of $BiVO_4$ through synergistic modifications in both structure and electronic properties, with distinct responses based on the target pollutant. This highlights the necessity of tailoring catalyst design to specific contaminant profiles.

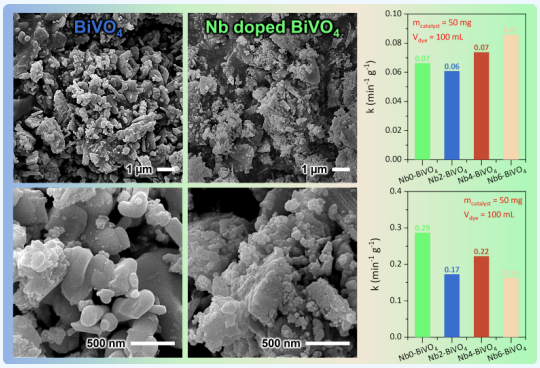

Keywords: *Nb-doped $BiVO_4$; photocatalysis; ciprofloxacin degradation; methylene blue; hydrothermal synthesis.*

1. INTRODUCTION

Semiconductor-based photocatalysis has garnered considerable attention for environmental remediation, particularly in the degradation of persistent organic pollutants in aqueous media [1, 2]. Among various visible-light-responsive materials, bismuth vanadate ($BiVO_4$) has emerged as a promising photocatalyst due to its appropriate band gap (~2.4 eV), chemical stability, and non-toxic nature [3, 4]. However, pristine $BiVO_4$ suffers from inherent drawbacks, including limited charge carrier mobility, rapid recombination of photoinduced electron-hole pairs, and relatively low surface area, all of which constrain its overall photocatalytic efficiency [5–7].

To overcome these limitations, several modification strategies have been investigated, such as heterojunction construction, surface functionalization, and elemental doping [8, 9]. Among these, doping with transition metals has proven to be an effective method for enhancing the photocatalytic activity of $BiVO_4$ by altering its electronic structure and facilitating improved charge separation [10]. In particular, niobium (Nb) has attracted attention as a dopant due to its similar ionic radius to Bi^{3+} and its capacity to serve as an electron donor when substituted into the $BiVO_4$ lattice [11, 12]. Prior studies suggest that Nb incorporation can reduce charge recombination, modulate band edge positions, and introduce beneficial defect states [11, 12]. Nevertheless, the influence of Nb doping on the morphology and surface chemistry of $BiVO_4$—key factors governing photocatalytic performance—remains insufficiently explored, especially in the context of pollutant-specific degradation behavior [13].

Furthermore, much of the existing literature emphasizes photocatalytic performance without establishing direct correlations between activity and the underlying physicochemical properties [14, 15]. A comprehensive understanding of how Nb doping simultaneously affects the crystal structure, surface morphology, optical absorption characteristics, and charge carrier dynamics is essential for the rational design of efficient $BiVO_4$-based photocatalysts. In addition, the role of surface texturing and its effect on pollutant adsorption, particularly for species with varying chemical functionalities, warrants further investigation.

In this work, Nb-doped $BiVO_4$ photocatalysts were synthesized via a hydrothermal route with varying Nb concen-

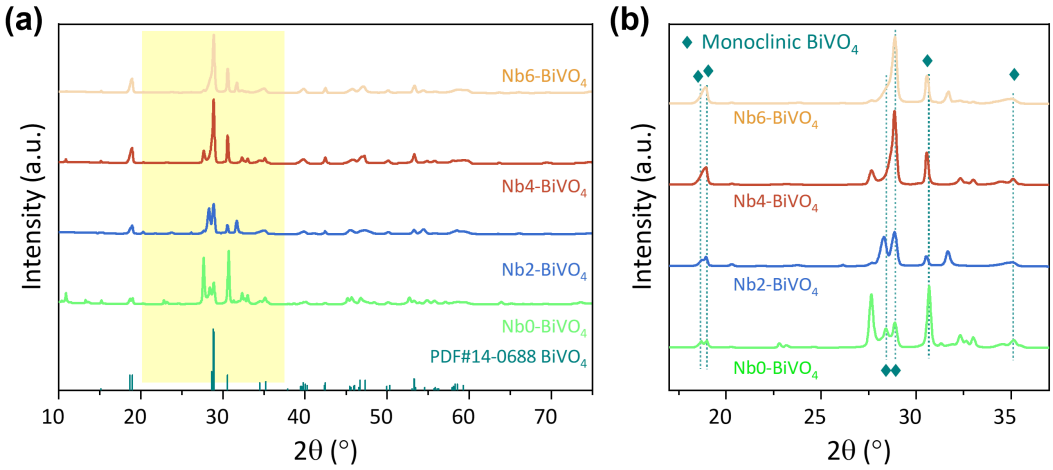

Figure 1. (a) X-ray diffraction (XRD) patterns of Nb-doped $BiVO_4$ with varying Nb content, highlighting the preservation of the monoclinic phase; (b) magnified view of the diffraction region between $2\theta = 17°$ and 37° showing minor reflections attributed to structural disorder or secondary phases.

trations ($X = 0$, 2, 4, and 6 mol%). The structural, morphological, and optical properties of the samples were systematically characterized. Photocatalytic activities were evaluated under UV irradiation using ciprofloxacin (CIP), a widely used antibiotic, and methylene blue (MB), a model cationic dye. By analyzing degradation kinetics in relation to material characteristics, this study aims to elucidate the dual contributions of electronic modulation and surface texturing induced by Nb doping, and their respective impacts on pollutant-specific photocatalytic efficiency.

2. MATERIALS AND METHODS

2.1 Materials

Bismuth(III) nitrate pentahydrate, $Bi(NO_3)_3{\cdot}5H_2O$ (reagent grade, crystals, ≥98%, Sigma-Aldrich), ammonium metavanadate, NH_4VO_3 (ACS reagent, ≥99.0%, Sigma-Aldrich), and ammonium niobate(V) oxalate hydrate, $C_4H_4NNbO_9{\cdot}xH_2O$ (99.99% trace metals basis, Sigma-Aldrich), were used as Bi, V, and Nb precursors, respectively. Methyl orange (C.I. 13025; pH indicator, ACS, Reag. Ph Eur) was employed as the model pollutant. Deionized (DI) water was used throughout all experiments. All chemicals were utilized as received, without further purification.

2.2 Preparation of Nb-Doped $BiVO_4$ Nanostructures

Undoped and Nb-doped $BiVO_4$ samples were synthesized via a hydrothermal method. Bismuth(III) nitrate pentahydrate (2.9 g in 50 mL DI water) and ammonium metavanadate (0.70 g in 30 mL DI water, gently heated to ~60 °C) were initially combined under constant stirring to yield a homogeneous Bi–V precursor solution. Ammonium niobate(V) oxalate hydrate was subsequently introduced into this mixture to achieve nominal Nb doping levels of 2%, 4%, and 6% (i.e., 0.089 g, 0.181 g, and 0.272 g, respectively). The resulting suspension was stirred for an additional 30 minutes to ensure full dissolution and uniform mixing. The prepared reaction mixture was transferred into a Teflon-lined stainless-steel autoclave, sealed, and subjected to hydrothermal treatment at 150 °C for 24 hours. After naturally cooling to room temperature, the solid products were recovered via vacuum filtration, thoroughly rinsed with deionized water, and dried in an oven at 80 °C for 2 hours. The dried powders were then calcined at 500 °C for 2 hours to enhance crystallinity and phase purity, as well as to remove residual organic species from the Nb precursor. The resulting samples are hereafter denoted as NbX-$BiVO_4$, where X represents the molar percentage of Nb incorporated during synthesis (i.e., Nb0-$BiVO_4$, Nb2-$BiVO_4$, Nb4-$BiVO_4$, and Nb6-$BiVO_4$).

2.3 Materials Characterizations

The morphology and microstructure of the synthesized samples were examined using field-emission scanning electron microscopy (FESEM; JEOL JSM-7610F) equipped with energy-dispersive X-ray spectroscopy (EDS) for semi-quantitative elemental analysis, including evaluation of Nb distribution. Crystalline phases were identified by X-ray diffraction (XRD; Rigaku SmartLab SE Basic) using Cu Kα radiation (λ = 1.5406 Å). Optical properties were investigated via UV-Vis spectroscopy (Shimadzu UV-1900, Japan), and Tauc plots were constructed to estimate the optical band gaps. Photoluminescence (PL) spectroscopy was conducted using a Shimadzu RF-5301 spectrophotometer (Japan) to assess charge-carrier recombination behavior, with emission intensities near ~560 nm compared across NbX-$BiVO_4$ samples.

2.4 Photodegradation Investigation

Photocatalytic activity was assessed in batch experiments (100 mL volume) using a catalyst loading of 50 mg (0.5 g/L). Initial pollutant concentrations were 10 ppm for ciprofloxacin (CIP) and 5 ppm for methylene blue (MB). The suspensions were stirred in the dark for 60 minutes to establish adsorption–desorption equilibrium, followed by UV irradiation using four 10 W Philips TUV lamps (253.7 nm wavelength) under continuous stirring at ambient temperature. At 30-minute intervals, approximately 3 mL aliquots were withdrawn, filtered through syringe filters to remove particulates, and analyzed via UV-Vis spectrophotometry (Shimadzu UV-1200). Pollutant concentrations were determined from calibration curves using characteristic absorption wavelengths of 271 nm for CIP and 663 nm for MB, respectively. Results were expressed as C/C_0 and used to evaluate degradation kinetics, including pseudo-first-order rate constant calculations where applicable.

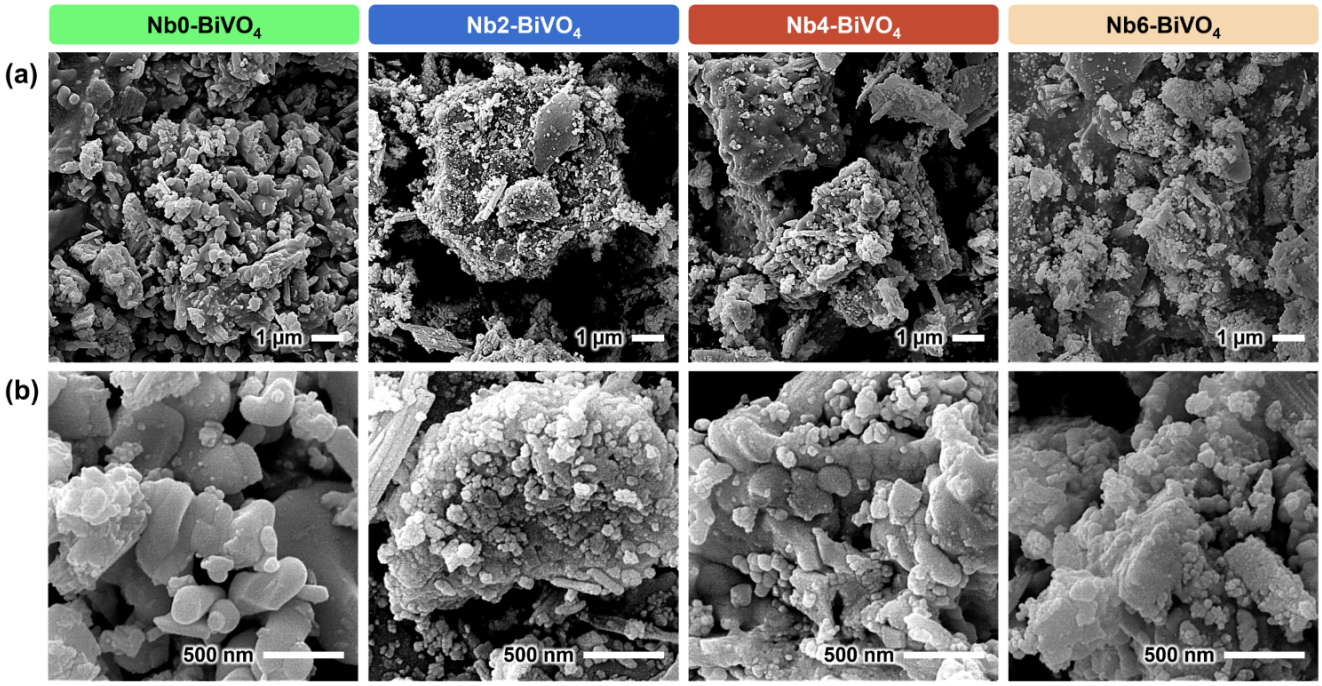

Figure 2. (a) Field-emission scanning electron microscopy (FESEM) images of Nb-doped $BiVO_4$ (Nb0, Nb2, Nb4, Nb6) at 10,000× magnification; (b) corresponding high-magnification views at 50,000×, highlighting surface evolution and nanoscale texturing with increasing Nb content.

Table 1. Elemental composition of Nb*X*-$BiVO_4$ (X = 0, 2, 4, 6) determined by FESEM-EDS, reported as wt% and at% for O, Bi, V, and Nb.

Element	Nb0-$BiVO_4$		Nb2-$BiVO_4$		Nb4-$BiVO_4$		Nb6-$BiVO_4$	
	wt%	at%	wt%	at%	wt%	at%	wt%	at%
Oxygen (O)	6.37	37.06	6.01	32.3	6.19	34.47	6.62	35.7
Bismuth (Bi)	78.25	34.84	63.74	26.24	66.18	28.24	62.18	25.68
Vanadium (V)	15.38	28.10	17.61	29.75	13.63	23.85	12.60	21.34
Niobium (Nb)	–	–	12.64	11.71	14.00	13.44	18.60	17.28

3. RESULTS AND DISCUSSION

Figure 1 presents the X-ray diffraction (XRD) patterns of Nb*X*-$BiVO_4$, illustrating the crystallographic features and phase composition of the synthesized materials. All samples display characteristic diffraction peaks corresponding to monoclinic scheelite $BiVO_4$, in agreement with the standard reference pattern (PDF #14-0688) [16], confirming this phase as the dominant component (Figure 1a). The most prominent peaks appear at $2\theta \approx 18.7°$, 28.9°, 30.5°, 34.5°, and 47.3°, which correspond to the (101), (112), (004), (200), and (204) planes, respectively [17].

Notably, several minor unidentified reflections are evident, particularly in the Nb-doped samples, as emphasized in the magnified region between $2\theta = 18°$ and 36° (Figure 1b). These additional peaks suggest the presence of secondary phases or structural inhomogeneities not associated with the ideal $BiVO_4$ lattice [18]. Their emergence, along with subtle variations in peak intensities and broadening, implies that Nb incorporation induces crystallographic disorder or results in incomplete phase development. These findings indicate that while the employed synthesis conditions successfully produce monoclinic $BiVO_4$ as the primary phase, they do not fully suppress impurity formation, particularly at elevated doping levels.

Figure 2 shows FESEM micrographs of Nb*X*-$BiVO_4$ acquired at magnifications of 10,000× and 50,000×, illustrating the morphological evolution as a function of Nb content. At lower magnification (Figure 2a), all samples appear as highly agglomerated clusters composed of submicron primary grains. The undoped sample (Nb0-$BiVO_4$) exhibits intergrown, plate-like structures with comparatively smooth surfaces [19]. In contrast, Nb-doped samples (Nb2-$BiVO_4$, Nb4-$BiVO_4$, and Nb6-$BiVO_4$) display increasingly rough and granular morphologies.

At higher magnification (Figure 2b), surface textures are observed in greater detail. Nb4-$BiVO_4$ features uniformly distributed hemispherical nodules, while Nb6-$BiVO_4$ exhibits dense, fine-scale surface asperities. The dimensions of these features range from tens to several hundreds of nanometers, whereas the underlying grain sizes remain approximately 200–500 nm. These findings suggest that Nb incorporation enhances surface roughness and nanoscale texturing, which

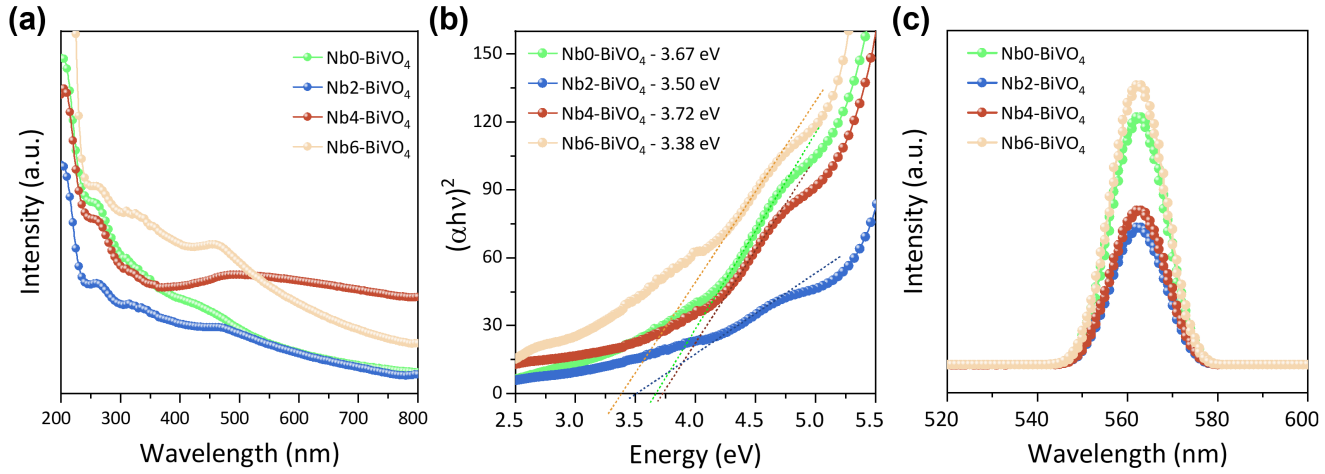

Figure 3. (a) UV–Vis absorption spectra of Nb-doped $BiVO_4$ (Nb0, Nb2, Nb4, Nb6), showing variations in absorption edge behavior; (b) corresponding Tauc plots ($(\alpha h\nu)^2$ vs. $h\nu$) used to estimate optical band gaps of approximately 3.67, 3.50, 3.72, and 3.38 eV for Nb0, Nb2, Nb4, and Nb6-$BiVO_4$, respectively; (c) photoluminescence (PL) emission spectra with broad emissions centered near 560 nm, indicating recombination characteristics.

may contribute to improved interfacial reactivity [20].

Table 1 presents the elemental composition of the synthesized samples as determined by FESEM-EDS, reported in both weight percent (wt%) and atomic percent (at%). As expected, Nb is not detected in the undoped sample (Nb0-$BiVO_4$), while its concentration increases with the doping level: 11.71 at% in Nb2-$BiVO_4$, 13.44 at% in Nb4-$BiVO_4$, and 17.28 at% in Nb6-$BiVO_4$. These values are consistent with the nominal Nb contents introduced during synthesis. Simultaneously, the atomic percentages of Bi and V decrease with increasing Nb content, suggesting partial substitution within the $BiVO_4$ lattice or possible surface enrichment of Nb. Oxygen content remains relatively constant (32–36 at%), though slightly below the stoichiometric value for $BiVO_4$—a common occurrence in EDS due to underestimation of light elements. The Bi:V atomic ratio exhibits modest variation across the samples, reflecting the semi-quantitative limitations of EDS analysis. Overall, these trends confirm successful Nb incorporation while also indicating potential structural or compositional heterogeneities induced during the doping process.

Figure 3 illustrates the optical and photoluminescence (PL) properties of Nb*X*-$BiVO_4$, highlighting the influence of Nb doping on light absorption behavior and charge carrier dynamics. The UV–Vis absorption spectra (Figure 3a) reveal strong absorption in the UV region for all samples, with visible-light absorption tails extending from the absorption edge. Compared to the undoped sample (Nb0-$BiVO_4$), Nb2-$BiVO_4$ and Nb6-$BiVO_4$ exhibit red-shifted absorption onsets and elevated baseline absorbance, whereas Nb4-$BiVO_4$ shows a slightly blue-shifted edge. These spectral variations suggest that Nb incorporation modifies the electronic structure, potentially by introducing localized states or perturbing band-edge transitions.

Tauc plots constructed from the absorption data (Figure 3b), assuming direct allowed transitions, yield estimated band gap energies of approximately 3.67, 3.50, 3.72, and 3.38 eV for Nb0-, Nb2-, Nb4-, and Nb6-$BiVO_4$, respectively [21, 22]. This non-monotonic trend indicates that low to moderate Nb doping initially narrows the band gap (Nb2), followed by a slight widening (Nb4), and then a pronounced reduction at higher doping levels (Nb6). These results confirm that Nb incorporation influences the optical band structure, enabling partial tuning of the absorption threshold.

The PL spectra (Figure 3c) further support the impact of Nb doping on charge carrier behavior. All samples exhibit broad emission centered near 560 nm, attributed to radiative recombination of photoexcited charge carriers. Notably, PL intensity decreases progressively with increasing Nb content, with Nb6-$BiVO_4$ showing the most pronounced quenching. This emission reduction implies enhanced charge separation or the presence of additional non-radiative recombination pathways in doped samples, both of which are favorable for photocatalytic activity [23, 24]. Overall, the optical and PL data demonstrate that Nb doping significantly affects both electronic transitions and recombination dynamics in $BiVO_4$, offering mechanistic insight into the observed enhancements in photocatalytic performance.

Figure 4 presents time-resolved UV–Vis spectra illustrating the photocatalytic degradation of ciprofloxacin (CIP; panels a–d) and methylene blue (MB; panels e–h) over Nb*X*-$BiVO_4$ under UV irradiation. For CIP degradation (0–120 min), the characteristic UV absorption bands progressively diminish over time. The spectral attenuation is most significant for Nb2-$BiVO_4$ and Nb6-$BiVO_4$, indicating enhanced photocatalytic performance relative to the undoped sample (Nb0-$BiVO_4$). Nb4-$BiVO_4$ exhibits an intermediate response. Similarly, MB degradation (0–180 min) is monitored by the decline in intensity of the Q-band centered near 665–670 nm. Substantial reductions in absorbance are observed for Nb2-$BiVO_4$ and Nb6-$BiVO_4$, approaching near-complete bleaching, while Nb0-$BiVO_4$ demonstrates the lowest activity. Again, Nb4-$BiVO_4$ shows a moderate response. These findings suggest that Nb doping, particularly at 2% and 6%, significantly enhances photocatalytic efficiency. This improvement aligns with previously discussed modifications in electronic structure and surface morphology, underscoring the synergistic contributions of Nb incorporation to photocatalytic activity.

Figure 5 presents the kinetic analysis of photocatalytic degradation of ciprofloxacin (CIP; panels a–c) and methylene blue (MB; panels d–f) using Nb*X*-$BiVO_4$ photocatalysts. For CIP degradation (Figure 5a), all samples demonstrate a sharp

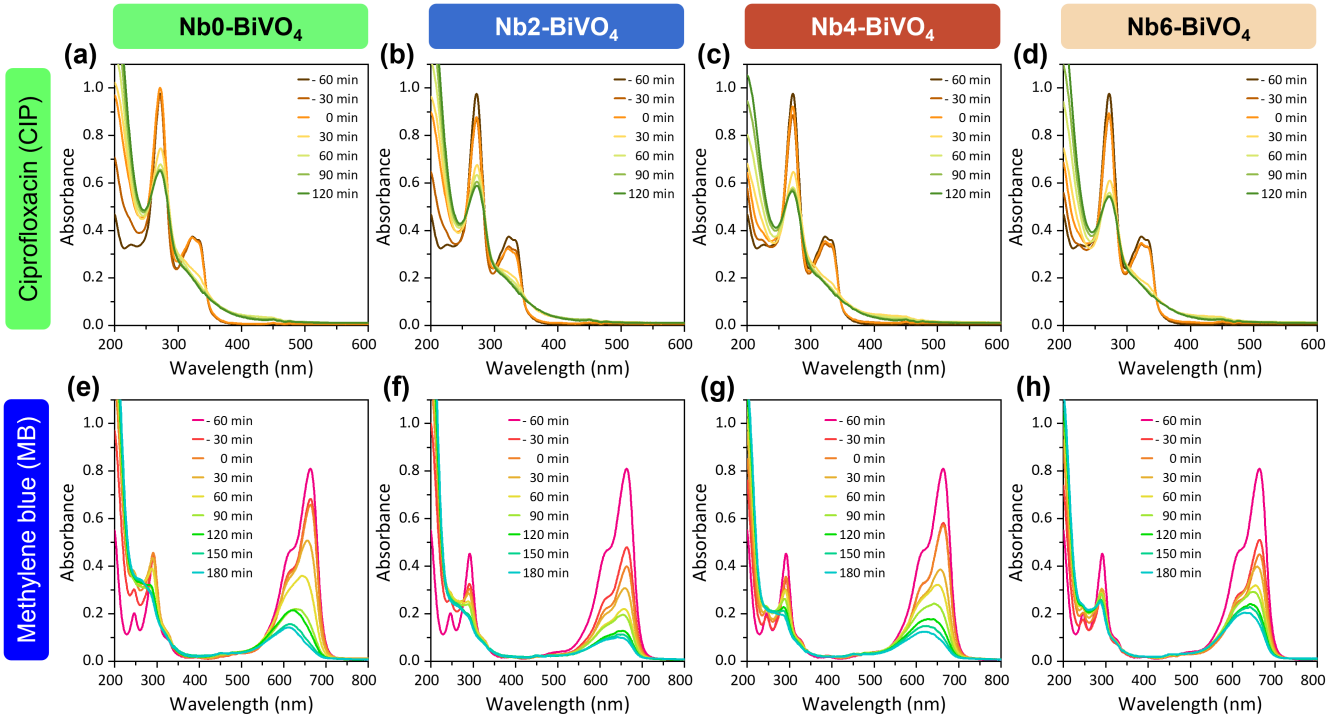

Figure 4. (a–d) UV–Vis absorption spectra of ciprofloxacin (CIP) during photocatalytic degradation using Nb*X*–$BiVO_4$: (a) Nb0, (b) Nb2, (c) Nb4, and (d) Nb6 over a 120-minute period. (e–h) UV–Vis absorption spectra of methylene blue (MB) under similar conditions: (e) Nb0, (f) Nb2, (g) Nb4, and (h) Nb6 over 180 minutes. Spectral decreases reflect degradation kinetics and photocatalytic efficiency.

decrease in concentration upon UV illumination following an initial 60-minute dark adsorption stage. The corresponding semi-logarithmic plots of $\ln(C_0/C)$ versus time (Figure 5b) exhibit linear behavior, confirming that the reaction follows pseudo–first-order kinetics under the employed conditions. The calculated mass-normalized rate constants (Figure 5c) indicate that Nb6-$BiVO_4$ achieves the highest degradation rate, followed by Nb4-$BiVO_4$ and Nb0-$BiVO_4$, which show nearly equivalent performance. Nb2-$BiVO_4$ displays the lowest activity. These trends align with optical data (Figure 3), where Nb6 doping resulted in the most pronounced band gap narrowing and photoluminescence (PL) quenching, indicative of enhanced charge separation.

For MB degradation (Figure 5d), a substantial concentration decrease occurs during the dark stage, suggesting stronger initial adsorption compared to CIP. The pseudo–first-order model remains applicable (Figure 5e); however, the rate constants (Figure 5f) differ significantly. Nb0-$BiVO_4$ exhibits the highest degradation rate, followed by Nb4-$BiVO_4$, while both Nb2-$BiVO_4$ and Nb6-$BiVO_4$ show reduced performance. This inverse trend highlights the pollutant-specific nature of photocatalytic behavior, where adsorption affinity and surface interactions may outweigh bulk electronic enhancements.

These findings reveal a clear pollutant-dependent performance pattern. For CIP, Nb6-$BiVO_4$ exhibits the highest pseudo–first-order rate constant, consistent with enhanced surface morphology and electronic properties. FESEM analysis (Figure 2b) shows that Nb6-$BiVO_4$ features increased nanoscale texture and surface roughness, which enhance the active surface area. Additionally, UV–Vis and PL results (Figure 3) confirm a narrowed band gap and suppressed recombination, promoting improved charge separation. These synergistic effects contribute to superior photocatalytic activity for CIP degradation. In contrast, MB degradation favors the undoped sample (Nb0-$BiVO_4$), which demonstrates the highest rate constant and strongest adsorption during the dark stage. This suggests that surface affinity plays a more dominant role in MB removal. The reduced performance of doped samples may result from altered surface chemistry, such as decreased hydroxyl group density or changes in surface charge, which diminish dye adsorption despite electronic improvements. Overall, while all samples retain the monoclinic $BiVO_4$ phase, Nb doping introduces significant morphological and electronic modifications that influence photocatalytic outcomes. These results emphasize the importance of aligning photocatalyst design with the chemical nature of the target pollutant to achieve optimal performance.

4. CONCLUSION

Nb-doped $BiVO_4$ photocatalysts were successfully synthesized via a hydrothermal route, and their structural, morphological, optical, and photocatalytic properties were systematically investigated. X-ray diffraction (XRD) analysis confirmed that the monoclinic $BiVO_4$ phase was retained across all samples, although minor unidentified reflections suggested partial crystallographic disorder or secondary phase formation, particularly at higher doping levels. Optical characterizations revealed that Nb doping influenced the electronic structure, as evidenced by shifts in the absorption edge and non-monotonic variations in estimated band gap energies. Photoluminescence (PL) spectra further indicated enhanced charge carrier separation, with emission quenching observed in Nb-doped samples. These findings confirm the dual role of Nb in

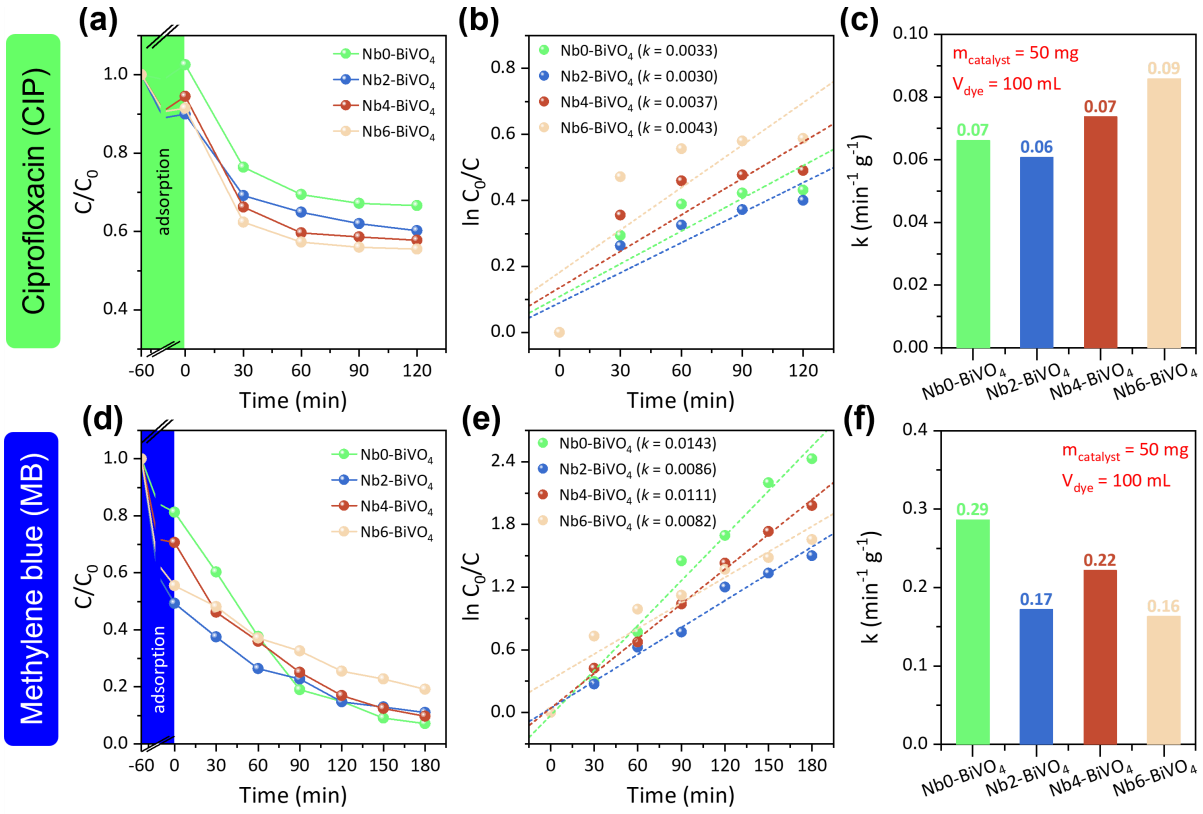

Figure 5. Photocatalytic degradation kinetics for ciprofloxacin (CIP) and methylene blue (MB) using NbX–$BiVO_4$ (X = 0, 2, 4, 6). (a, d) Temporal concentration profiles (C/C_0) under UV irradiation, following a 60-minute dark adsorption period (indicated by shading). (b, e) Pseudo–first-order kinetic plots of $\ln(C_0/C)$ versus time, with fitted rate constants k provided in the legends. (c, f) Bar charts comparing k values normalized per gram of catalyst, illustrating performance trends across dopant levels and pollutants.

modifying both band structure and recombination dynamics. Photocatalytic tests demonstrated pollutant-specific activity profiles. For ciprofloxacin (CIP), Nb6-$BiVO_4$ exhibited the highest degradation rate, attributable to its increased surface area and efficient charge separation. Nb4-$BiVO_4$ and Nb0-$BiVO_4$ showed comparable performance, while Nb2-$BiVO_4$ displayed the lowest activity. In contrast, methylene blue (MB) degradation was more strongly influenced by surface adsorption properties. The undoped $BiVO_4$ outperformed all Nb-doped variants, indicating that surface affinity rather than electronic enhancement governed MB removal efficiency. These results highlight that Nb doping enhances photocatalytic activity through synergistic morphological and electronic effects, yet the extent of improvement is highly dependent on the physicochemical characteristics of the target pollutant.

DATA AVAILABILITY STATEMENT

The datasets generated during and/or analyzed during the current study are available from the corresponding author on reasonable request.

CONFLICT OF INTEREST

The authors declare that there are no conflicts of interest associated with this publication, and there has been no significant financial support for this work that could have influenced its outcome.

REFERENCES

[1] M. N. Subramaniam, P. S. Goh, D. Kanakaraju, J. W. Lim, W. J. Lau, A. F. Ismail, Photocatalytic membranes: a new perspective for persistent organic pollutants removal, Environmental Science and Pollution Research 29 (2022) 12506–12530. https://doi.org/10.1007/s11356-021-14676-x.

[2] T. E. Doll, F. H. Frimmel, Removal of selected persistent organic pollutants by heterogeneous photocatalysis in water, Catalysis Today 101 (2005) 195–202. https://doi.org/10.1016/j.cattod.2005.03.005.

[3] B. Patial, A. Bansal, R. Gupta, S. K. Mittal, $Bivo_4$-based heterojunction nanophotocatalysts for water splitting and organic pollutant degradation: a comprehensive review of photocatalytic innovation, Reviews in Inorganic Chemistry 44 (2024) 495–519. https://doi.org/10.1515/revic-2024-0009.

[4] S. Lotfi, M. El Ouardi, H. A. Ahsaine, A. Assani, Recent progress on the synthesis, morphology and photocatalytic dye degradation of $bivo_4$ photocatalysts: A review, Catalysis Reviews 66 (2024) 214–258. https://doi.org/10.1080/01614940.2022.2057044.

[5] N. T. K. Huyen, T.-D. Pham, N. T. D. Cam, P. V. Quan, N. V. Noi, N. T. Hanh, M. H. T. Tung, V.-D. Dao, Fabrication of titanium doped $bivo_4$ as a novel visible light driven photocatalyst for degradation of residual tetracycline pollutant, Ceramics International 47 (2021) 34253–34259. https://doi.org/10.1016/j.ceramint.2021.08.335.

[6] C. Regmi, Y. K. Kshetri, R. P. Pandey, T.-H. Kim, G. Gyawali, S. W. Lee, Understanding the multifunctionality in cu-doped $bivo_4$ semiconductor photocatalyst, Journal of Environmental Sciences 75 (2019) 84–97. https://doi.org/10.1016/j.jes.2018.03.005.

[7] C. Regmi, Y. K. Kshetri, T.-H. Kim, R. P. Pandey, S. W. Lee, Visible-light-induced fe-doped $bivo_4$ photocatalyst for contaminated water treatment, Molecular Catalysis 432 (2017) 220–231. https://doi.org/10.1016/j.mcat.2017.02.004.

[8] B. Guan, J. Chen, Z. Li, Z. Zhuang, Y. Chen, Z. Ma, J. Guo, C. Zhu, X. Hu, S. Zhao, et al., Review on synthesis, modification, morphology, and combination of $bivo_4$-based catalysts for photochemistry: Status, advances, and perspectives, Energy & Fuels 38 (2024) 806–853. https://doi.org/10.1021/acs.energyfuels.3c03932.

[9] J. Liu, B. Li, L. Kong, Q. Xiao, S. Huang, Surfactants-assisted morphological regulation of $bivo_4$ nanostructures for photocatalytic degradation of organic pollutants in wastewater, Journal of Physics and Chemistry of Solids 172 (2023) 111079. https://doi.org/10.1016/j.jpcs.2022.111079.

[10] A. Zhang, Y. Liang, H. Zhang, Z. Geng, J. Zeng, Doping regulation in transition metal compounds for electrocatalysis, Chemical Society Reviews 50 (2021) 9817–9844. https://doi.org/10.1039/D1CS00330E.

[11] W. Yan, X. Liu, Niobium-doped tio_2: Effect of an interstitial oxygen atom on the charge state of niobium, Inorganic Chemistry 58 (2019) 3090–3098. https://doi.org/10.1021/acs.inorgchem.8b03096.

[12] E. Santos, A. C. Catto, A. F. Peterline, W. Avansi Jr, Transition metal (nb and w) doped tio_2 nanostructures: The role of metal doping in their photocatalytic activity and ozone gas-sensing performance, Applied Surface Science 579 (2022) 152146. https://doi.org/10.1016/j.apsusc.2021.152146.

[13] B. N. Nunes, W. van den Bergh, F. Strauss, A. Kondrakov, J. Janek, T. Brezesinski, The role of niobium in layered oxide cathodes for conventional lithium-ion and solid-state batteries, Inorganic Chemistry Frontiers 10 (2023) 7126–7145. https://doi.org/10.1039/D3QI01857A.

[14] H. P. Sarker, P. M. Rao, M. N. Huda, Niobium doping in $bivo_4$: Interplay between effective mass, stability, and pressure, ChemPhysChem 20 (2019) 773–784. https://doi.org/10.1002/cphc.201800792.

[15] S. S. Kalanur, H. Seo, An experimental and density functional theory studies of nb-doped $bivo_4$ photoanodes for enhanced solar water splitting, Journal of Catalysis 410 (2022) 144–155. https://doi.org/10.1016/j.jcat.2022.04.019.

[16] K. Ren, J. Zhou, Z. Wu, Q. Sun, L. Qi, Dual heterojunctions and nanobowl morphology engineered $bivo_4$ photoanodes for enhanced solar water splitting, Small 20 (2024). https://doi.org/10.1002/smll.202304835.

[17] Q. Sun, L. Yang, F. Hu, C. Liang, H. Wang, J. Qi, Microstructural evolution and kinetics of monoclinic scheelite-type $bivo_4$-based materials with enhanced color performance, Ceramics International 51 (2025) 40414–40430. https://doi.org/10.1016/j.ceramint.2025.06.276.

[18] C. Cheng, H. Tan, W. Zhu, L. Liu, K. Chen, J. Yan, The transition of tetragonal to monoclinic phase in $bivo_4$ coupled with peroxymonosulfate for photocatalytic degradation of tetracycline hydrochloride, Environmental Research 267 (2025) 120631. https://doi.org/10.1016/j.envres.2024.120631.

[19] S. S. Kalanur, Y. J. Lee, H. Seo, A versatile synthesis strategy and band insights of monoclinic clinobisvanite $bivo_4$ thin films for enhanced photoelectrochemical water splitting activity, Applied Surface Science 562 (2021) 150078. https://doi.org/10.1016/j.apsusc.2021.150078.

[20] Y. Zou, M. Lu, Z. Jiang, L. Xu, C. Liu, L. Zhang, Y. Chen, Hydrothermal synthesis of zn-doped $bivo_4$ with mixed crystal phase for enhanced photocatalytic activity, Optical Materials 119 (2021) 111398. https://doi.org/10.1016/j.optmat.2021.111398.

[21] S. Saxena, A. Verma, N. K. Biswas, S. A. Khan, V. R. Satsangi, R. Shrivastav, S. Dass, Zr–w co-doping in $bivo_4$ – synergistic effect in photoelectrochemical water splitting, Materials Chemistry and Physics 267 (2021) 124675. https://doi.org/10.1016/j.matchemphys.2021.124675.

[22] N. Singh, U. Kumar, N. Jatav, I. Sinha, Photocatalytic degradation of crystal violet on cu, zn doped $bivo_4$ particles, Langmuir 40 (2024) 8450–8462. https://doi.org/10.1021/acs.langmuir.3c04039.

[23] S. Tekin, Y. Tutel, A. Karatay, H. E. Unalan, A. Elmali, Defect assisted enhanced nonlinear optical performance and optical limiting of pure and doped $bivo_4$ powders and nanocomposite films, Journal of Luminescence 252 (2022) 119362. https://doi.org/10.1016/j.jlumin.2022.119362.

[24] D. Channei, P. Thammaacheep, S. Kerdphon, P. Jannoey, W. Khanitchaidecha, A. Nakaruk, Domestic microwave-assisted synthesis of pd doped-$bivo_4$ photocatalysts, Inorganic Chemistry Communications 150 (2023) 110478. https://doi.org/10.1016/j.inoche.2023.110478.

